

On the nonlinear theory of the long-wavelength radiative condensation instability

B. Meerson

Racah Institute of Physics, Hebrew University of Jerusalem, 91904 Jerusalem, Israel

C. D. C. Steele, A. M. Milne, and E. R. Priest

Department of Mathematical and Computational Sciences, University of St. Andrews, St. Andrews KY16 9SS, Scotland

(Received 17 February 1993; accepted 26 April 1993)

Nonlinear evolution of the radiative condensation instability (RCI) of an optically thin plasma is investigated in the framework of a one-dimensional model. The model is applicable for motions either along a sufficiently strong magnetic field, when the transverse heat conduction is suppressed, or perpendicular to a straight, shear-free magnetic field. The long-wavelength limit of the RCI is considered when the characteristic radiative cooling time is much shorter than the acoustic (or magnetoacoustic) time. The case when the isochoric thermal mode is damped, while one of the two “acoustic” (or “magnetoacoustic”) modes is unstable, is studied. Two different problems of the instability are considered. In the first, the heat conduction is negligible and the instability is described by a reduced set of equations, which formally coincide with those of a gas whose effective compressibility as a function of the density is of alternating sign. The study starts with small perturbations and follows them numerically into the nonlinear regime. It is shown that, during the first stage of the instability, cool plasma condensations develop, these being surrounded by rarefied and hot plasma regions. Subsequently the condensations expand unless mass inflow into the system is disallowed. The condensation boundaries represent a new type of shock wave which develops in such a “normal-anomalous” gas dynamics. These shock waves have a monotonic density profile, but a nonmonotonic pressure profile. Properties of the shock waves are investigated analytically and numerically. If the mass inflow is disallowed, stable equilibrium condensations develop, the boundaries of which represent contact discontinuities. In the second problem, the heat conduction is relatively large, so that direct crossover between the long-wavelength limit and the heat conduction-dominated short-wavelength limit occurs. In this case also either static or expanding plasma condensations are shown to develop, depending on the boundary conditions. An analytical description of the static equilibria is presented.

I. INTRODUCTION

Radiative condensations are a general phenomenon often found when optically thin plasmas cool radiatively. Interstellar¹ and intergalactic² clouds, solar prominences³ and “marfes” in tokamaks⁴ represent relatively cool, dense plasma structures, which are surrounded by hotter rarefied plasmas and strongly radiate. Also, radiative effects are important in many dynamic phenomena in laboratory plasmas, for example, in radiating Z-pinches.⁵ The radiative condensation instability (RCI), arising because of the interplay between external heating, radiative cooling, heat conduction and plasma motions, has long been invoked as a mechanism for the formation of radiative condensations in various applications,⁶⁻⁹ and it has been extensively studied, analytically and numerically, starting from the pioneering work by Field,⁷ where a consistent linear theory of the RCI was developed. Since then, many more linear studies and several numerical¹⁰⁻¹⁶ and analytical¹⁷⁻²² nonlinear investigations have been performed in various contexts. It has been shown that the instability is normally strong, and its saturated states (normally in the form of strongly nonlinear, standing or moving structures, or patterns) are very different from the initial one.

Recently, some progress in studying the nonlinear behavior of the RCI in a general context has been made possible, as different sets of simplified, reduced equations have been suggested for different limiting cases. The reduced equations have helped to gain an insight into the physical nature of the nonlinear RCI (still poorly understood), to find analogs of the RCI in other physical systems, and in some cases to obtain informative analytical solutions.

The different limiting cases are present due to the presence of different characteristic time scales (and related spatial scales) in the problem of the RCI. For example, in the simplest case of an unmagnetized plasma with no external fields, these are the radiative (τ_r), acoustic (τ_a) and heat-conduction (τ_c) time scales. The same time scales persist in the case of plasma motion along a sufficiently strong magnetic field, when the heat conduction across the field is negligible. In the case of motions across a straight-line shear-free magnetic field, the relevant time scales are the radiative, magnetoacoustic (τ_{ma}) and transverse heat-conduction times. The radiative time scale is independent of the (typical) perturbation wave number k , whereas the (magneto-) acoustic and heat-conduction time scales are

inversely proportional to k and to k^2 , respectively.

In the most thoroughly studied intermediate- and short-wavelength limits, the acoustic time scale is the shortest, therefore a uniform pressure sets in rapidly. Corresponding reduced equations were suggested and employed for different problems in Refs.18–23.

On the contrary, it is the radiative time scale which is the shortest in the long-wavelength limit. Then, the complete thermal balance equation can be replaced by an algebraic condition of local thermal equilibrium. This procedure reduces the problem of the long-wavelength RCI to that of the dynamics of a gas whose “effective” pressure is a nonmonotonic function of the gas density, which ensures negative compressibility of the gas over some range of densities.^{17,21,24} If this range of densities is very large, one can formally extend the negative compressibility over the whole range of densities. Such an idealized problem was investigated analytically¹⁷ in a one-dimensional geometry (see also Ref. 25 and references therein for many mathematically similar problems arising in other contexts). It was shown¹⁷ that, on a finite time scale, the flow generally develops localized singularities (infinitely dense and cold states, and infinitely rarefied and hot states). In a three-dimensional geometry, the corresponding problem appears to be similar to the well-known problem of nonlinear gravitational instability,²⁴ so that formation of flattened plasma condensations (“thermal pancakes”) at a strongly nonlinear stage of the RCI was predicted.¹⁷

The problem involving a realistic, alternate-sign compressibility has not been considered yet. As similar sets of equations have also arisen in other contexts, this problem is quite universal and deserves attention. Also, when the plasma heat conduction is relatively large, so that the heat conduction and radiative cooling time scales are comparable to each other, but much shorter than the (magneto-) acoustic time scale, direct crossover between the long-wavelength and short-wavelength limits occurs, the theory of which is not available yet.

The problem involving a realistic, alternate-sign compressibility has not been considered yet. As similar sets of equations have also arisen in other contexts, this problem is quite universal and deserves attention. Also, when the plasma heat conduction is relatively large, so that the heat conduction and radiative cooling time scales are comparable to each other, but much shorter than the (magneto-) acoustic time scale, direct crossover between the long-wavelength and short-wavelength limits occurs, the theory of which is not available yet.

The aim of the present paper is the analytical and numerical analysis of these two problems in a general context. The paper is organized in the following way. In Sec. II we present two sets of nonlinear reduced equations: (i) for the long-wavelength RCI and (ii) for the direct crossover regime; and we briefly review the corresponding linear theories. In Sec. III we employ the long-wavelength reduced equations and study analytically the contact discontinuities and shock waves in such a “normal-anomalous” gas dynamics. In Sec. IV we solve the same equations numerically for different parameters and boundary and initial conditions and compare the results with our theory. Section V is devoted to the analytical and numerical investigation of the direct crossover regime of the RCI. Section VI contains a brief summary and discussion of the results.

II. REDUCED EQUATIONS

Let us consider a one-dimensional flow of an optically thin plasma, which is heated by some external agent and cooled radiatively. We start with the usual continuity, Navier–Stokes and thermal balance equations

$$\frac{d\rho}{dt} + \rho \frac{\partial v}{\partial x} = 0, \quad (1)$$

$$\rho \frac{dv}{dt} = -\frac{\partial p}{\partial x} + \eta \frac{\partial^2 v}{\partial x^2}, \quad (2)$$

$$\frac{1}{\gamma-1} \frac{dp}{dt} + \frac{\gamma}{\gamma-1} \rho \frac{\partial v}{\partial x} + \rho \mathcal{L}(\rho, T) - \frac{\partial}{\partial x} \left(K \frac{\partial T}{\partial x} \right) = 0, \quad (3)$$

and equation of state

$$p = \frac{R}{\mu} \rho T, \quad (4)$$

where $d/dt = \partial/\partial t + v\partial/\partial x$ is the total time derivative, \mathcal{L} is the heating–cooling function (the difference between the rate of radiative cooling and the rate of heating per unit mass), $K = K(T)$ is the thermal conductivity, η is the viscosity, γ is the specific heat ratio, μ is effective molar mass of the plasma, R is the gas constant, and the rest of notation is conventional.

Equations (1)–(3) are valid for a planar flow of an unmagnetized plasma, or for a plasma flow along a sufficiently strong magnetic field, when the transverse heat conduction is negligible. This model is a reasonable approximation for the RCI in tokamak plasma¹⁴ and for the problem of formation of prominences in the solar atmosphere.^{12,13,26} The form of function $\mathcal{L}(\rho, T)$ is determined by specific mechanisms of heating and cooling and varies from one application to another.

In order to delineate different limiting cases and introduce the necessary notation, we shall briefly reiterate, with a minor extension, the relevant results of the linear theory of the RCI.⁷ The problem of linear stability of uniform equilibria of the set of equations (1)–(4), $\rho = \rho_0 = \text{const}$, $T = T_0 = \text{const}$, $v = 0$ and $\mathcal{L}(\rho_0, T_0) = 0$, can be reduced to the analysis of a cubic dispersion relation for the complex frequency, so that for a fixed perturbation wave number k there are always three modes, which can generally be stable, unstable or overstable. Let us introduce two characteristic length scales, the acoustic Field length, $\lambda_a = c_s \tau_r$, and heat conductive Field length, $\lambda_c = (\kappa \tau_r)^{1/2}$, where c_s is the speed of sound and $\kappa = K/\rho$ is the thermal diffusivity of the plasma. The long-wavelength limit corresponds to $k \ll \min(\lambda_a^{-1}, \lambda_c^{-1})$. In this limit, the three above-mentioned modes are the “isochoric” mode, the growth (or damping) rate of which is generally nonzero, while the real part of the frequency is zero as $k \rightarrow 0$, and two “acoustic” modes, whose frequencies both tend to zero as $k \rightarrow 0$. When the isochoric instability criterion is satisfied $(\partial \mathcal{L} / \partial T_0)_\rho < 0$, the two remaining modes represent propagating acoustic waves, strongly modified by the heating–cooling effects. In the opposite case $(\partial \mathcal{L} / \partial T_0)_\rho > 0$, the “acoustic” modes become non-propagating (one of the modes purely growing, the other damped), if the isobaric instability criterion is satisfied:

$$\left(\frac{\partial \mathcal{L}}{\partial T_0} \right)_\rho = \left(\frac{\partial \mathcal{L}}{\partial T_0} \right)_\rho - \frac{\rho_0}{T_0} \left(\frac{\partial \mathcal{L}}{\partial \rho_0} \right)_T < 0. \quad (5)$$

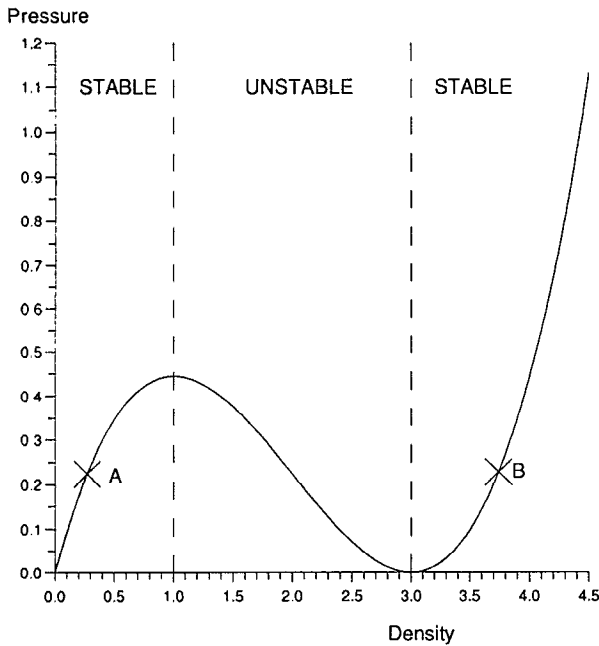


FIG. 1. An example of the effective pressure $P(\rho)$, showing “negative gas compressibility” on the interval (1,3).

(Here, and in the following, the subscript “0” in a derivative means that the derivative is evaluated in equilibrium.) Since the radiative loss rate in a plasma grows with ρ (like ρ^2), the second term in Eq. (5) is usually destabilizing. We shall consider the case when the isochoric criterion is not satisfied (otherwise, the system would “jump” rapidly, on the radiative time scale, from the isochorically unstable state to an isochorically stable one¹⁷), while the isobaric one is satisfied. Let us start with an arbitrary small-amplitude long-wavelength perturbation around a uniform equilibrium. Those parts of the perturbation corresponding to the isochoric mode will be damped out rapidly, on the radiative time scale. The following evolution of the perturbation proceeds on a much longer, acoustic time scale, and it can be approximately described by the long-wavelength reduced equations.^{17,24} To obtain these equations, one should replace the complete thermal balance equation (3) by the thermal equilibrium condition

$$\mathcal{L}(\rho, T) = 0. \quad (6)$$

Solving the algebraic equation (6) for $T = T_*(\rho)$ and substituting it into Eq. (4), we obtain the plasma pressure

$$p = (R/\mu)\rho T_*(\rho) = P(\rho),$$

which is a function of the density only, so that Eqs. (1) and (2) with the effective pressure $p = P(\rho)$ represent a closed set. These are the long-wavelength reduced equations for the RCI of an isochorically stable plasma.^{17,24} It was shown by Pikel’ner,⁸ that the effective pressure P of an optically thin, radiating plasma with a cosmic abundance of elements, and which is heated by UV-radiation and sub-cosmic rays, is a nonmonotonic function of the density (like that shown in Fig. 1), which can lead to instability.

The same reduced equations (1) and (2) with a different form for the effective pressure $P(\rho)$ arise in the long-wavelength limit of the RCI of planar plasma motions perpendicular to a straight magnetic field.²¹ This model seems to be applicable for hot regions of the interstellar and intergalactic plasmas,^{1,27} where high longitudinal heat conduction rapidly erases any perturbations along the magnetic field. At the same time, as the parameter $\beta = 8\pi p/B^2$ in the interstellar plasma is of the order of or larger than unity,²⁷ the (frozen-in) magnetic field B can be deformed significantly by the perpendicular plasma motions, while the stabilizing effect of the magnetic pressure on the RCI⁷ can be insufficient to quench the instability. This problem is described by the reduced equations (1) and (2) with the effective pressure²¹

$$P(\rho) = p + \frac{B^2}{8\pi} \frac{R}{\mu} \rho T_*(\rho) + \frac{B_0^2}{8\pi\rho_0} \rho^2, \quad (7)$$

where B_0 is the unperturbed uniform magnetic field. As the magnetic field is frozen into the plasma, it can be expressed in terms of the plasma density [as has been done in Eq. (7)], as long as the instability develops from a uniform equilibrium. Therefore, the second term on the right-hand side of Eq. (7) grows with density and describes the stabilizing effect of the magnetic field perpendicular to the plasma motion.

Linearizing the reduced equations near the equilibrium $\rho = \rho_0$ and $v = 0$, and looking for solutions in the form of $\exp(nt + ikx)$, we obtain

$$n = \pm k \left(-\frac{dP}{d\rho_0} + \frac{\nu^2 k^2}{4} \right)^{1/2} - \frac{\nu k^2}{2}, \quad (8)$$

where $\nu = \eta/\rho_0$ is the unperturbed kinematic viscosity. It can be seen from Eq. (8), that a necessary and sufficient condition for the instability of one of the “acoustic” modes is

$$\frac{dP}{d\rho_0} < 0, \quad (9)$$

which formally means negative gas compressibility. The viscosity reduces the growth rate, but it is unable to quench the instability. An example of the effective pressure, for which the instability can develop, is shown in Fig. 1, where density intervals (0,1) and (3, ∞) are stable, while interval (1,3) is unstable (normalized density and pressure units are used). The linear growth rate (8) increases monotonically with k and becomes saturated, approaching $-\nu^{-1}dP/d\rho_0$ as $k \rightarrow \infty$.

Of course, these linear results coincide with the long-wavelength asymptotics of the “complete” linear theories of the RCI in the two above-mentioned problems.⁷ To prove it, we return to the heating-cooling function $\mathcal{L}(\rho, T)$ and calculate $dP/d\rho_0$ at $\mathcal{L} = \text{const}$. For the case of an unmagnetized plasma or plasma moving along a strong magnetic field we obtain from Eq. (8):

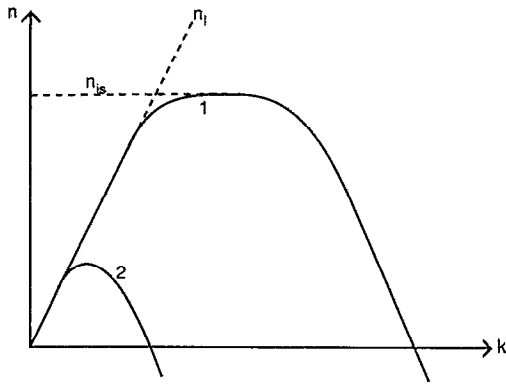


FIG. 2. The linear growth rates of the RCI versus the perturbation wave number k , and its asymptotics. Curve 1 corresponds to the case of $\lambda_c \ll \lambda_a$, while curve 2 corresponds to the opposite inequality.

$$n_l = \pm kc_i \left\{ - \left[\left(\frac{\partial \mathcal{L}}{\partial T_0} \right)_\rho - \frac{\rho_0}{T_0} \left(\frac{\partial \mathcal{L}}{\partial \rho_0} \right)_T \right] / \left(\frac{\partial \mathcal{L}}{\partial T_0} \right)_\rho \right\}^{1/2}, \quad (10)$$

where we put $\nu=0$ and $c_i^2 = RT_0/\mu$. Equation (10) coincides with the long-wavelength asymptotics, $k \ll \min(\lambda_a^{-1}, \lambda_c^{-1})$, of the general expression for the linear growth rate.⁷ It is seen from Eq. (10), that the instability criterion $dP/d\rho_0 < 0$ is equivalent to the two following inequalities:

$$\left(\frac{\partial \mathcal{L}}{\partial T_0} \right)_\rho > 0 \quad \text{and} \quad \left(\frac{\partial \mathcal{L}}{\partial T_0} \right)_p = \left(\frac{\partial \mathcal{L}}{\partial T_0} \right)_\rho - \frac{\rho_0}{T_0} \left(\frac{\partial \mathcal{L}}{\partial \rho_0} \right)_T < 0, \quad (11)$$

i.e., the isochoric stability and isobaric instability criteria. Note, however, that the instability itself is not isobaric in this limit, the pressure varying both in space and in time.

Similarly, the linear growth rate predicted by the reduced equations coincides with that following from the general linear theory of the RCI developing across the magnetic field. In this case, the criterion (9) for instability of one of the "magnetoacoustic" modes implies: (i) $(\partial \mathcal{L}/\partial T)_\rho > 0$ (isochoric stability); and (ii) $(\partial \mathcal{L}/\partial T)_{p_{\text{tot}}} < 0$, where $p_{\text{tot}} = p + B^2/8\pi$ is the total (thermal + magnetic) pressure.

The linear increase of the growth rate n with the wave number k , predicted by Eq. (10) with $\nu=0$, terminates at $k \sim \min(\lambda_a^{-1}, \lambda_c^{-1})$, i.e., outside the long-wavelength limit. If $\lambda_c \ll \lambda_a$ and $k \gg \lambda_a^{-1}$, we arrive at the intermediate- and short-wavelength limits, and the linear growth rate becomes⁷

$$n_{is} = \frac{(\gamma-1)\mu}{\gamma R} \left\{ - \left[\left(\frac{\partial \mathcal{L}}{\partial T_0} \right)_\rho - \frac{\rho_0}{T_0} \left(\frac{\partial \mathcal{L}}{\partial \rho_0} \right)_T \right] - \kappa_0 k^2 \right\}, \quad (12)$$

where $\kappa_0 = K(T_0)/\rho_0$ is the unperturbed thermal diffusivity. It is the force equilibrium, rather than thermal equilibrium, which sets in first in this regime, so that the plasma pressure remains approximately uniform. Figure 2 (curve 1 and its two asymptotics) shows schematically the dependence of the linear growth rate on k for the case of $\lambda_c \ll \lambda_a$, when all three ranges, the long-, intermediate- and short-wavelength ones, are well pronounced. Shown is the plot of $n=n(k)$ and its asymptotics n_l and n_{is} from Eqs. (10) and (12), respectively. It is seen that the long-wavelength range is well described by the linearized reduced equations (1) and (2) with an effective pressure $p=P(\rho)$. Similarly, we expect that the nonlinear reduced equations should describe well the nonlinear long-wavelength RCI as long as $\lambda_c \ll \lambda_a$.

In addition to the long-wavelength limit of the RCI, Eqs. (1) and (2) [with a nonmonotonic effective pressure $p=P(\rho)$, like that shown in Fig. 1] describe other physical systems.²⁵ The best known of them is the van der Waals model for real gases, for which the equation of state is²⁸

$$p(\rho, T) = \frac{8T\rho}{3-\rho} - 3\rho^2, \quad (13)$$

where all the quantities (pressure, density and temperature) are related to their critical values. For $T < 1$, the pressure is a nonmonotonic function of ρ , the falling part of which corresponds to the instability of the overcooled vapor. If one "quickly" prepares (for instance, in a Wilson cloud chamber) a uniform equilibrium state of such a vapor, its subsequent (isothermal) instability will be similar to the long-wavelength RCI.

Now let us proceed to the case of a large heat conduction, so that $\lambda_a \ll \lambda_c$. In this case the perturbation wavelength can become comparable to λ_c . In other words, the radiative cooling time τ_r becomes comparable to the heat conduction time τ_c , but both of them are small compared to the (magneto-) acoustic time τ_a . In this case, a balance between the heat conduction and heating-cooling effects, rather than a local thermal equilibrium, will set in rapidly:

$$\rho \mathcal{L}(\rho, T) - \frac{\partial}{\partial x} \left(K \frac{\partial T}{\partial x} \right) = 0, \quad (14)$$

and then a slower evolution will proceed on the (magneto-) acoustic time scale. Corresponding "direct crossover equations" include Eqs. (1), (2), (4) and (14). In contrast to the complete thermal balance equation (3), relation (14) does not contain any time derivative, which leads to a reduction of the order of the system.

The linear theory, following from the direct crossover equations, predicts the following growth rate:

$$n_{dc} = \pm kc_i \left(- \frac{(\partial \mathcal{L}/\partial T_0)_\rho - (\rho_0/T_0)(\partial \mathcal{L}/\partial \rho_0)_T + \kappa_0 k^2}{(\partial \mathcal{L}/\partial T_0)_\rho + \kappa_0 k^2} \right)^{1/2} \quad (15)$$

where we put $\nu=0$. The same result follows from the general dispersion equation⁷ in the limit of $k \ll \lambda_a^{-1}$ and $\lambda_a \ll \lambda_c$. The growth rate (15) as a function of k is shown in Fig. 2 (curve 2). It can be seen that for large enough k there is no instability, while the maximum growth rate is much smaller than that predicted by Eq. (12). The long-wavelength regime in this case is followed directly by the short-wavelength one, while the intermediate-wavelength regime is absent. The long-wavelength linear growth rate (10) can be restored from Eq. (15) in the limit $\kappa_0 k^2 \rightarrow 0$.

The direct crossover model is also valid for the one dimensional RCI perpendicular to a strong magnetic field.²¹ We only have to replace the plasma pressure p by the total pressure p_{tot} , which is now a function of ρ and T (the frozen-in magnetic field can still be expressed in terms of the plasma density, if we start from a uniform equilibrium).

In the following sections we shall employ the two systems of reduced equations to study the nonlinear evolution of the RCI.

III. NORMAL-ANOMALOUS GAS DYNAMICS AND SHOCK WAVES

The similarity between the problem of the nonlinear long-wavelength RCI and the problem of the isothermal dynamics of the van der Waals gas gives a hint about possible final states. In the van der Waals gas, the instability results in segregation of the overcooled vapor into two phases: the liquid and the "normal" vapor, which coexist in an inhomogeneous state.²⁸ As we are unaware of any time-dependent theory for such a segregation, the following results might be also useful for the van der Waals model. Note that, while the reduced equations (1) and (2) with the effective pressure $p=P(\rho)$ describe the RCI in the long-wavelength limit only, the same equations for the isothermic van der Waals gas do not have this limitation.

Let us start with possible equilibria of the long-wavelength reduced equations, described by the conditions $v=0$ and $\partial/\partial t=0$, from which follows $\partial p/\partial x=0$. Homogeneous equilibria, $\rho=\rho_0=\text{const}$, are stable if ρ_0 corresponds to a rising part of the $P(\rho)$ -curve, unstable for a falling part of the $P(\rho)$ -curve and neutral at the extremum points of $P(\rho)$. The rising branches of the curve $P(\rho)$ imply "normal" gas dynamics, when a small initial perturbation of a uniform equilibrium gives rise (for a small viscosity) to propagating acoustic waves. On the contrary, the falling parts of $P(\rho)$ correspond to "anomalous" gas dynamics, when a small perturbation of a uniform equilibrium results in instability: the perturbation grows in time and remains localized.^{17,25} It is known that the convective nonlinearities in Eqs. (1) and (2) are unable to saturate the instability (actually, they usually accelerate it). Therefore, it was suggested¹⁷ that the final, segregated state of the system would be very different from the initial state, while the nonlinear saturation would be related to the pressure buildup, arising when localized "tongues" of high- and low-density plasma penetrate the stable, rising branches of the $P(\rho)$ -curve. Of course, at the strongly non-

linear stage a dissipation mechanism (like viscosity or heat conduction) is necessary to avoid wave-breaking.

The simplest segregated states are contact discontinuities. For such an equilibrium the density "jumps" from, say ρ_1 to $\rho_2 > \rho_1$ at some point x_0 , while the pressure remains uniform: $P(\rho_1)=P(\rho_2)$. This equilibrium is obviously impossible if both ρ_1 and ρ_2 belong to the same rising or falling branches of the $P(\rho)$ -curve [just as it is impossible in the case of a "normal," that is growing, $P(\rho)$]. However, it becomes possible when ρ_1 , and ρ_2 belong to different rising branches of $P(\rho)$, while $P(\rho_1)=P(\rho_2)$, as at the points A and B in Fig. 1. In the problem of the RCI such a contact discontinuity represents an equilibrium boundary between the cool and dense plasma on one side and the hot and rarefied plasma on the other. In the van der Waals model, it is the equilibrium boundary between the coexisting liquid drop and normal vapor.

A natural generalization of the discontinuous equilibria are propagating shock waves, which are described by traveling wave solutions of the long-wavelength reduced equations. As the plasma velocity in this solution is non-zero, the viscosity will determine a finite width of the shock front.

Looking for traveling wave solutions, $\rho(x,t)=\rho(\xi)$ and $v(x,t)=v(\xi)$, where $\xi=x-ct$ and c is the wave speed, we arrive at the following equations:

$$\rho(v-c) = \rho_1(v_1-c) = \rho_2(v_2-c), \quad (16)$$

$$\rho(v-c) \frac{dv}{d\xi} = -\frac{dP}{d\xi} + \eta \frac{d^2v}{d\xi^2}, \quad (17)$$

with the boundary conditions $\rho=\rho_2$, $v=v_2$ at $\xi=-\infty$, and $\rho=\rho_1$, $v=v_1$ at $\xi=+\infty$. Using Eq. (16) and integrating Eq. (17) once, taking account of the boundary conditions, we obtain

$$\eta c_0 \rho_2 \frac{d}{d\xi} \left(\frac{1}{\rho} \right) = -P(\rho) + P_2 - c_0^2 \frac{\rho_2^2}{\rho} + c_0^2 \rho_2, \quad (18)$$

where

$$(v_2-c)^2 = c_0^2 = \frac{P_2 - P_1}{\rho_2 - \rho_1} \frac{\rho_1}{\rho_2}, \quad (19)$$

$$(v_1-c)^2 = \frac{P_2 - P_1}{\rho_2 - \rho_1} \frac{\rho_2}{\rho_1}, \quad (20)$$

and $P_{1,2}=P(\rho_{1,2})$. Also, from Eqs. (19) and (20)

$$(v_1 - v_2)^2 = \frac{(P_2 - P_1)(\rho_1 + \rho_2)}{\rho_1 \rho_2}. \quad (21)$$

It follows from any of Eqs. (19)–(21) that if $\rho_2 > \rho_1$ then $P_2 > P_1$. Formally speaking, the same inequality, as well as relations (18)–(21), hold also for "normal" gas dynamics.²⁹ An important difference, however, is the fact that the inequality $P_2 > P_1$ can be achieved now not only on the same rising branches of the $P(\rho)$ -curve, but also on its different rising branches. Therefore, shock waves with a monotonic density profile, but a nonmonotonic pressure profile, are possible. The front of such an "anomalous" shock wave represents a narrow unstable density region

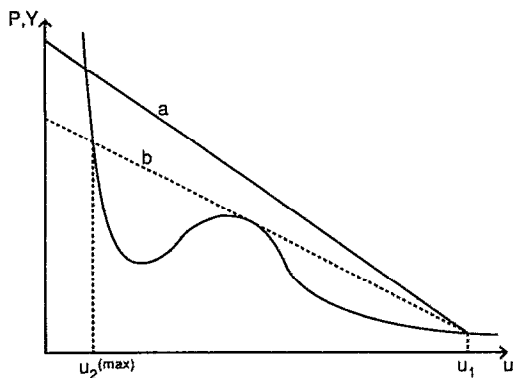


FIG. 3. A graphical analysis of the positiveness of the function $F(u)$ from Eq. (22), giving, for a fixed u_1 , allowable values of u_2 . The curve represents the graph of the effective pressure $P(1/u)$, while the straight lines a and b represent the function $Y(u)$ from Eq. (24) for a typical allowable value of u_2 (a), and for the maximum allowable value of u_2 (b).

confined by two stable regions of higher and lower density. As a consequence, a small pressure difference $P_2 - P_1$ in the anomalous shock wave may correspond to a large density ratio ρ_2/ρ_1 , which results in a relatively small value of c_0 and therefore in a narrow shock front [see Eq. (18), where the shock front width is seen to be proportional to c_0].

Another important difference between the “normal” and “anomalous” shocks becomes clear if we try to integrate Eq. (18) and find the density profile $\rho = \rho(\xi)$ of the shock wave. Introducing the specific volume $u = \rho^{-1}$, we rewrite Eq. (18) as

$$\frac{\eta c_0}{u_2} \frac{du}{d\xi} = F(u) \equiv P_2 - \frac{P_2 - P_1}{u_2 - u_1} (u - u_2) - P\left(\frac{1}{u}\right), \quad (22)$$

where $u_{1,2} = \rho_{1,2}^{-1}$. The function $F(u)$ vanishes at $u = u_1$ and $u = u_2$. The solution of Eq. (22) can be written in an implicit form as

$$\frac{u_2}{\eta c_0} \xi = \int_{u_2}^u \frac{du'}{F(u')} + \text{const.} \quad (23)$$

For this to describe a shock wave with a monotonic density profile, the function $F(u)$ must be positive at all internal points of the interval (u_2, u_1) . This criterion holds automatically in “normal” gas dynamics, but needs to be addressed in our case. It can be conveniently checked if we analyze graphically the relative position of the curve $P(1/u)$ and the straight line $Y(u)$ passing through the points (u_1, P_1) and (u_2, P_2) :

$$Y(u) = P_2 - \frac{P_2 - P_1}{u_1 - u_2} (u - u_2). \quad (24)$$

Positiveness of the function $F(u)$ is achieved if the curve $P(1/u)$ and the straight line $Y(u)$ do not intersect inside the interval (u_2, u_1) . For a given u_1 , the maximum possible u_2 (that is, the minimum possible ρ_2) can be found from the condition of the straight line $Y(u)$ being an “upper” tangent to the curve $P(1/u)$, as shown in Fig. 3.

Once the above conditions are met, integration in Eq. (23) gives a desired traveling wave solution for any pre-

scribed function $P(\rho)$ and any admissible pair of ρ_1 and ρ_2 (see the next section for an example of such an integration). However, similar to “normal” gas dynamics, two more conditions have to be checked, in order that the anomalous shock wave be stable with respect to small perturbations in the direction of wave propagation. These are the “evolutionarity” conditions²⁹ requiring the shock wave to move (i) supersonically relatively to the gas in front of the shock, and (ii) subsonically relatively to the gas behind the shock. Landau (see Ref. 29) obtained these conditions from stability arguments only, comparing the number of independent parameters n_1 characterizing an arbitrary, small initial perturbation of a shock to the number of equations n_2 relating these parameters. It appears that, only if the two evolutionarity conditions (i) and (ii) are satisfied, we have $n_1 = n_2$, and the shock wave is stable. It is important, that these arguments do not invoke any thermodynamic considerations, and so they remain valid in our case of “normal-anomalous” gas dynamics. In our notation, the evolutionarity conditions can be written as a double inequality:

$$\frac{\rho_1}{\rho_2} \left(\frac{dP}{d\rho_1} \right)^{1/2} < c_0 < \left(\frac{dP}{d\rho_2} \right)^{1/2}, \quad (25)$$

where $dP/d\rho_{1,2}$ means $dP/d\rho$ evaluated at $\rho = \rho_{1,2}$.

Therefore, among the “elementary objects” of the “normal-anomalous” gas dynamics equations describing the long-wavelength limit of the RCI, there are propagating shock waves and (standing) contact discontinuities. In the next section, we solve the long-wavelength reduced equations numerically and find the role of these solutions in evolutionary problems.

IV. NORMAL-ANOMALOUS GAS DYNAMICS: NUMERICAL SIMULATIONS

The numerical solution of Eqs. (1) and (2) can be undertaken with a wide variety of methods. We had to choose a scheme, which would model both the localized instability and the shock wave formation and propagation. Therefore, care had to be taken to ensure that the dissipation required by the numerical scheme for stability was not so large as to inhibit the expected unstable growth of perturbations. In view of all this, we chose the Flux Corrected Transport method of Boris and Book,³⁰ a robust nonlinear advection algorithm [we added the viscosity term of Eq. (2) as an explicit source], which modifies the numerical diffusion terms locally to ensure numerical stability. A second “antidiffusive” set of fluxes is then applied subject to the constraint that the magnitude of the flux is modified to ensure that no new maxima or minima are created in the solution. Thus numerical instabilities were suppressed.

We adopted a simple cubic polynomial for $P(\rho)$:

$$P(\rho) = \frac{\rho^3}{9} - \frac{2}{3} \rho^2 + \rho, \quad (26)$$

so that

$$\frac{dP}{d\rho} = \frac{1}{3}(\rho - 1)(\rho - 3). \quad (27)$$

The graph of $P(\rho)$ is shown in Fig. 1. The region of instability is $1 < \rho < 3$. The computational interval was $0 < x < 2\pi$. Two types of sets of boundary conditions were used. In the first type, plasma inflow to the system (or outflow from the system) was allowed from both boundaries (an "open" system), and we prescribed a fixed value of the density and a zero velocity gradient at each boundary. These boundary conditions simulate the presence of large "reservoirs" of plasma on both sides of the region of interest, like chromospheric plasma "reservoirs" in the problem of solar prominence formation in a coronal loop.²⁶ In the second type of boundary conditions, plasma inflow and outflow were not allowed (a "closed" system), so that the density gradient and plasma velocity were set zero at each boundary. These boundary conditions imply mass conservation and simulate confined plasmas, so that they seem reasonable for tokamaks¹⁴ for instance.

We started with different initial conditions, mainly in the form of a small density or velocity perturbation around a uniform equilibrium $\rho = \rho_0$. The density perturbation was taken symmetric with respect to $x = \pi$:

$$\rho(x, t=0) = \rho_0 - \epsilon \cos(kx), \quad (28)$$

while the initial velocity was zero. Alternatively, the velocity perturbation described a localized symmetric plasma inflow to the central region and therefore had an antisymmetric form:

$$v(x, t=0) = v_0(x - \pi) \exp[-b(x - \pi)^2], \quad (29)$$

with b usually equal to 5, while the initial density was uniform and equal ρ_0 .

If the uniform equilibrium $\rho = \rho_0$ was stable [rising branches of the $P(\rho)$ -curve], we saw propagation of acoustic waves and their damping by viscosity. For unstable equilibria [falling branches of the $P(\rho)$ -curve], we observed localized instability, as predicted. Since at fixed ρ_0 and v the linear growth rate (8) increases with wave number k , it was difficult to follow the evolution of modes with a small k , since narrow secondary peaks (emerging because of nonlinearities and numerical errors) became dominant. On the contrary, modes with sufficiently large k could be conveniently studied as the linear growth rate for large k approached a plateau, see Eq. (8), so that the secondary peaks did not interfere. We followed the evolution of the mode $k=4$ in the case of a closed system for the initial conditions (28) with $\rho_0 = 1.2$, $\epsilon = 0.001$ and different viscosities. As the effective pressure $P(\rho)$ is smaller in the region with an increased density, inflow of the plasma into this region starts, so the density there keeps growing. Figure 4 shows the mode amplitude (plotted logarithmically) versus time for three different values of the viscosity. It can be seen that, after a short time (necessary for the system to develop a velocity perturbation consistent with the growing density perturbation), the mode growth enters the exponential stage predicted by the linear theory. The growth rates agree with those predicted by Eq. (8) with an accuracy of 2% to 3% for every value of η . Later, the evolution enters a nonlinear stage, when the mode amplitude first grows faster than in the linear stage (as predicted by

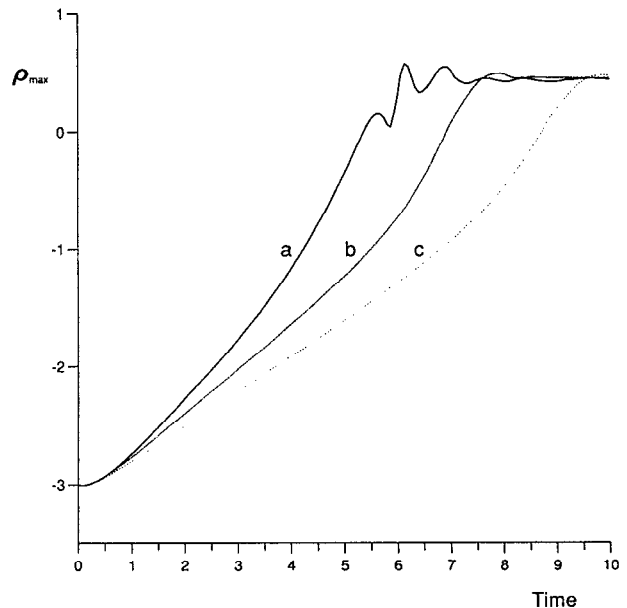


FIG. 4. Nonlinear evolution of the RCI in the long-wavelength limit for the no-flux boundary conditions. Shown is the decimal logarithm of the maximum density versus time for the initial condition (28) with $\rho_0 = 1.2$, $\epsilon = 0.001$ and $k = 4$. The viscosity $\eta = 0.04$ (curve a), 0.1 (curve b) and 0.16 (curve c).

"anomalous" gas dynamics^{17,25}), and then, after some oscillations, it becomes saturated. Figure 5 shows the evolution of the spatial profile of the same mode $k=4$ for $\eta = 0.1$. It can be seen that stable nonuniform equilibrium condensations finally develop. As the plasma velocity vanishes at the final stage and the pressure becomes constant (not shown graphically), this result means that the plasma

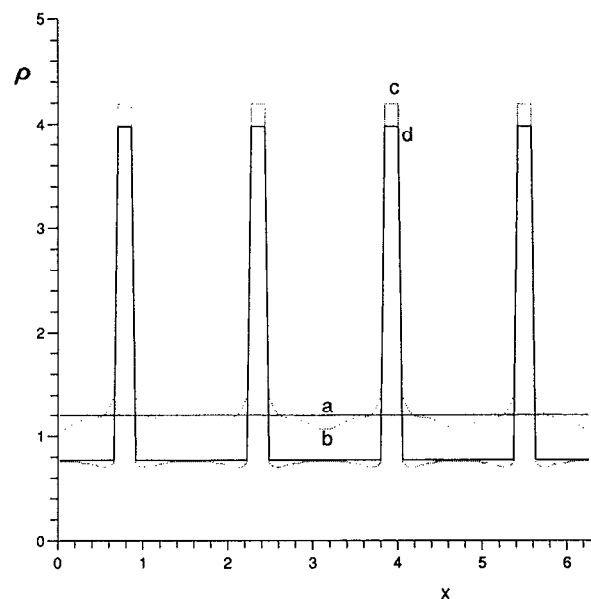


FIG. 5. Nonlinear evolution of the RCI in the long-wavelength limit. Shown is the density profile versus time for the times $t = 0$ (a), 6 (b), 8 (c), and 40 (d). The viscosity $\eta = 0.1$, and other conditions are the same as in Fig. 4.

is cool inside the condensations and hot outside. The condensation boundaries clearly represent contact discontinuities, considered in the previous section. It is important to note that this stable equilibrium was made possible by disallowing any mass supply to the system. As the total mass of the system is conserved in this case, the density away from the condensation has decreased to make up for the condensation formation. The process of formation of contact discontinuities remained intact for larger viscosities as well. In these cases, the condensation formation proceeded slower [as the linear growth rate (8) decreased], but residual velocities were damped faster.

Of a particular interest are the neutral stability points of the $P(\rho)$ -curve, where the linear growth rate (8) vanishes, so that the dynamics is governed by nonlinearities from the very beginning. In our simulations with an open system we chose such a point, $\rho_0 = 1$, and started from the small velocity perturbation (29) with $v_0 = 0.1$. The viscosity was $\eta = 0.1$. Figures 6(a) and 6(b) show the density and velocity profiles at different times. The small initial inflow of gas to the center leads to a slight increase in the density there ($t = 5$). By this time the effects of the (non-linear) instability become apparent. As the pressure in the central region remains smaller than that to either side, the plasma inflow into the central region continues until a narrow plasma condensation is formed so that the plasma pressure increases sufficiently to stop the compression. However, because of the flow inertia, the plasma condensation process and pressure buildup at the central region continue, so that an excessively large pressure is achieved there ($t = 10$ to 20). Because of this, a second stage of the process develops ($t = 20$ to 50), when the condensation starts to expand. The boundaries of the expanding condensation represent two shock waves with very narrow fronts, traveling away from the center and separating the stable higher and lower density regions. Simultaneously, the material is evacuated from the lower density periphery to the expanding condensation. By the time $t = 50$, the high density region has expanded to fill almost half the region of interest, while the pressure in the higher and lower density regions is uniform (and different). Note that, because of the neutral linear stability of the initial equilibrium, the time it takes for the instability to develop is longer than in the case of a linearly unstable equilibrium. Also, since the viscosity was relatively small in this run, the flow inertia was significant, and oscillatory motions of the fluid, clearly seen in Fig. 6(b) for the velocity, persisted for some time, so that no regime of steady expansion had been achieved yet by $t = 50$, when the run was terminated.

Another run [Figs. 7(a) and 7(b)] shows the effects of a larger viscosity in the same simulations with an open system (in this case $\eta = 0.5$). The same two stages are clearly seen: formation of plasma condensation by the instability, and its subsequent expansion in the form of two traveling shock waves with narrow fronts, representing a monotonic transition between the higher and lower density stable regions with uniform pressures. An obvious effect of the larger viscosity was to increase the growth time of the condensation. Also, the larger viscosity smoothed out vari-

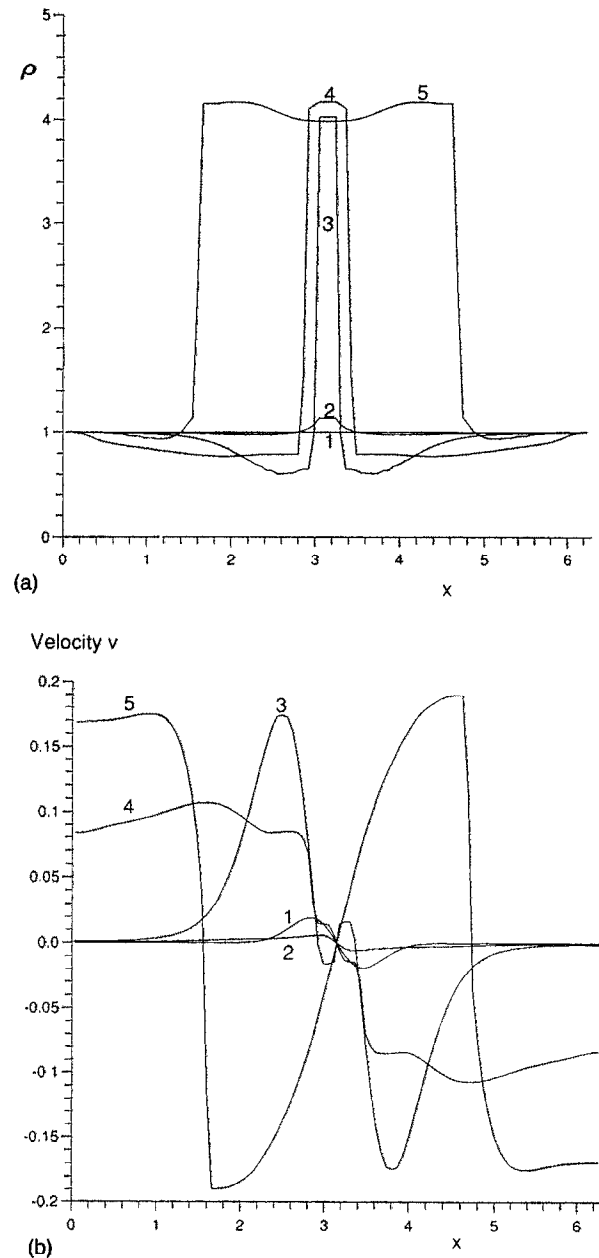


FIG. 6. Nonlinear evolution of the RCI in the long-wavelength limit for boundary conditions allowing plasma inflow. The initial equilibrium density $\rho_0 = 1.0$ corresponds to the neutral linear stability. Shown are the density (a) and velocity (b) profiles versus time for the initial condition (29) with $v_0 = 0.1$. The viscosity $\eta = 0.1$. The evolution is shown at successive time moments $t = 0$ (1), 5 (2), 10 (3), 20 (4) and 50 (5).

ations of the velocity and accelerated relaxation of the system to the steady expansion regime ($t = 200$ to 300).

A typical density evolution in the case of a closed system with a neutrally stable equilibrium is shown in Fig. 8 where we started with a small density perturbation (28) with $\rho_0 = 1$, $k = 1$ and $\epsilon = 0.01$, and took $\eta = 0.1$. The initial stage of instability and condensation formation looks similar to the previous cases. However, as the plasma inflow is disallowed, the expansion stops, and a stable condensation pattern is formed in a manner similar to the case of linearly unstable initial conditions considered before. Again, the

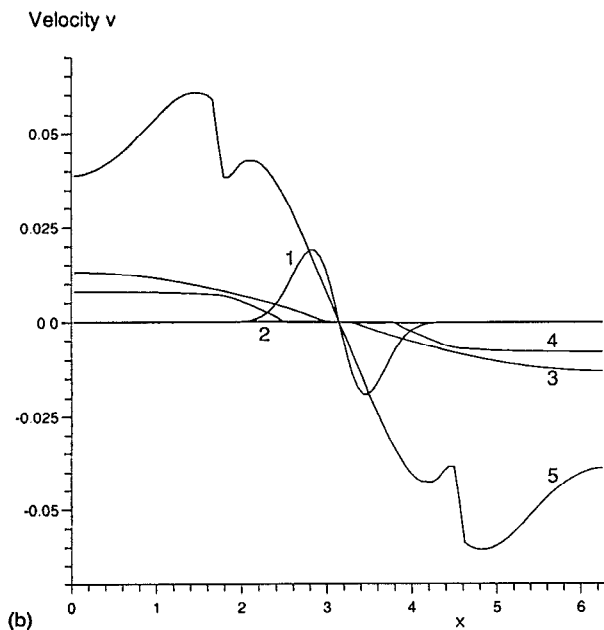
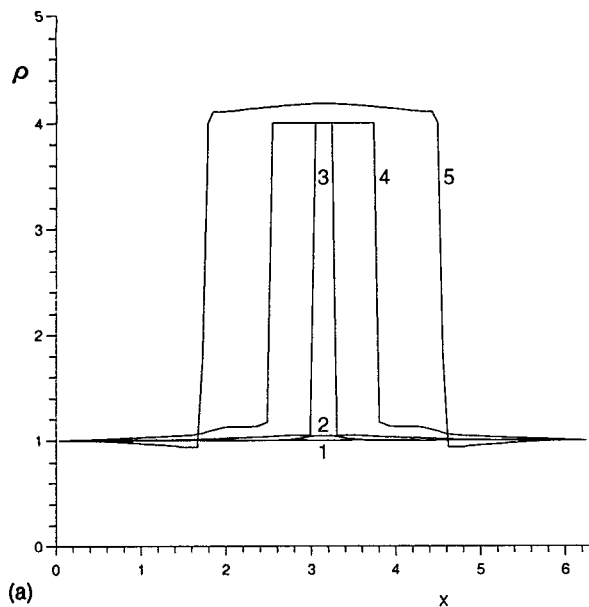


FIG. 7. The same as in Fig. 6, but $\eta=0.5$ and the times shown are $t=0$ (1), 50 (2), 100 (3), 200 (4) and 300 (5).

condensation boundaries represent contact discontinuities.

As our numerical simulations with the open system suggest that the anomalous shock waves, considered in the previous section, are indeed important in the long-time dynamics of the instability, we performed special numerical experiments to study the shock waves separately. We considered an open system and started with a discontinuity of the plasma density, $\rho=\rho_l$ at $x<x_0$, and $\rho=\rho_r$ at $x>x_0$, such that ρ_l and ρ_r were on the higher and lower density stable branches of the $P(\rho)$ -curve, respectively, while the initial velocity was zero. The higher density region $x<x_0$ was chosen to be at a higher pressure than the lower density region, so that the discontinuity was expected to move into the lower pressure region, that is from

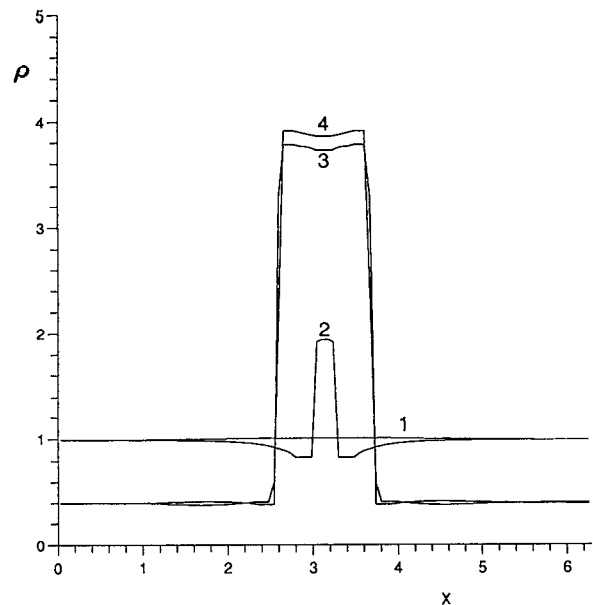


FIG. 8. Nonlinear evolution of the RCI in the long-wavelength limit for the no-flux boundary conditions. The initial equilibrium density $\rho_0=1.0$ corresponds to the neutral linear stability. Shown is the density profile versus time for the initial condition (28) with $k=1$ and $\epsilon=0.01$. The viscosity $\eta=0.1$. The evolution is shown at successive times $t=0$ (1), 50 (2), 100 (3), and 400 (4).

left to right. Since the initial values of the densities and zero velocities on the both sides of the discontinuity do not satisfy any particular traveling-wave solution, the discontinuity must, in general, break into several discontinuities, propagating in both directions, before each of them approaches a corresponding traveling-wave solution.

To save computation time, we started with a density discontinuity close to the left boundary. Therefore, only those discontinuities which propagate from left to right were expected to settle down and form a traveling-wave solution. A typical case of such an experiment is shown in Fig. 9, where the densities ρ_l and ρ_r were chosen to be 4.9 and 0.5 (corresponding to pressures of 1.97 and 0.35, respectively), x_0 was taken to be 5, and the viscosity was $\eta=0.1$. This time we used a much longer spatial interval, $0<x<24\pi$ to allow the system more time to evolve before being influenced by the right-hand boundary conditions. Shown in Fig. 9 are the density profiles at different times. It is seen that, after some irregular transient stage, the discontinuity “adjusts” a new value of the density on the left, $\rho_2=4.4$, and then propagates with almost a constant speed. To the right of the wave, the plasma remains static, while to the left, there is flow to the right, providing the plasma for the wave front to move. Equations (19) and (20) link the difference between the traveling wave speed c and the plasma velocities adjacent to the front, v_1 and v_2 , with the densities and pressures to either side of the front. Figure 10 shows separately the time evolution of the square roots of the left- and right-hand sides of Eq. (20) in this run. Shown in solid is the computed velocity difference $c-v_1$, while in broken is the function

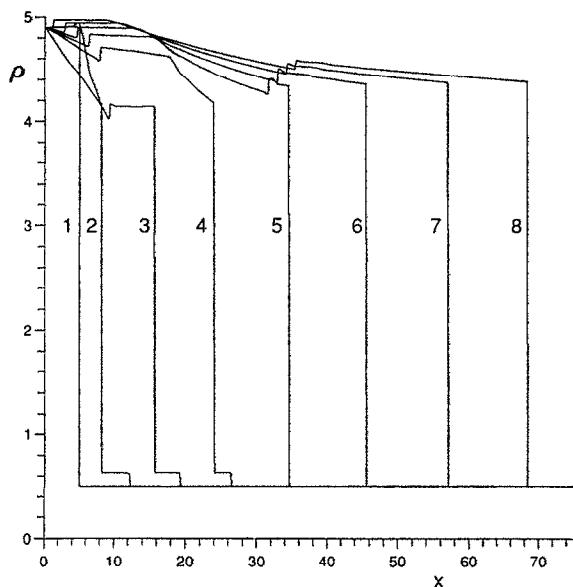


FIG. 9. Evolution of an arbitrary discontinuity of the density, as described by the long-wavelength equations for the RCI. At the time moment $t=0$ (profile 1) a discontinuity is prescribed with $\rho_l=4.9$ and $\rho_r=0.5$. At subsequent times $t=10, 20, 30, \dots, 70$ (profiles 2–8) the propagating discontinuity is adjusting itself and evolving into an anomalous shock wave.

$$\Delta = \left(\frac{P_2 - P_1}{\rho_2 - \rho_1} \frac{\rho_2}{\rho_1} \right)^{1/2}$$

It is seen that, starting from $t = 36$, the two curves show quite a good agreement.

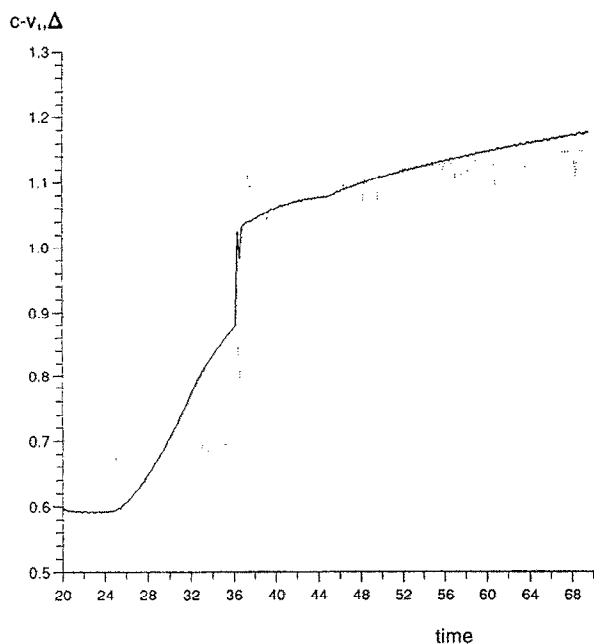


FIG. 10. Comparison of the shock wave speed from Fig. 9 with its theoretical value. Shown in solid is the computed velocity difference $c-v_1$, while in broken is the function Δ .

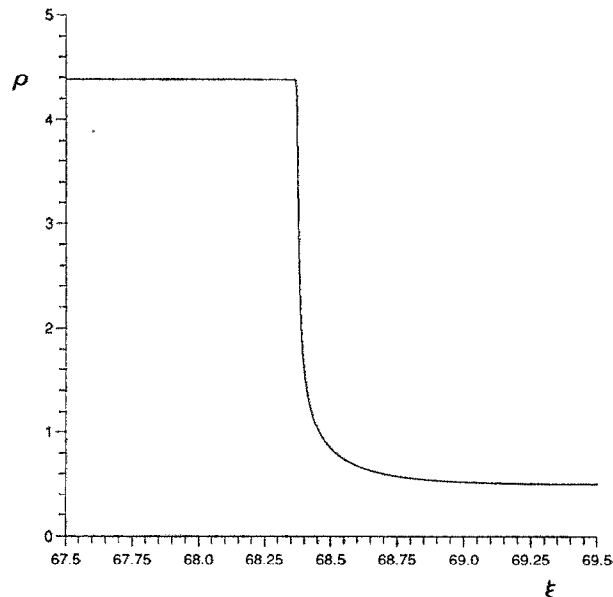


FIG. 11. The density profile of the anomalous shock wave, as predicted by the theory [Eq. (18)]. Parameters are the following: $\rho_1=0.5$, $\rho_2=4.384$ and $\eta=0.25$.

Also, we checked that the propagating shock wave finally developing in Fig. 9 satisfies the two evolutionarity conditions (25). It can be also seen directly from Fig. 9, where, starting from $t=40$, no perturbation is present on the right of the shock wave, while a small acoustic perturbation on the left, arising close to $t=40$, remains almost immobile, that it moves to the left in the shock wave's reference frame.

Finally, we solved Eq. (18) for the shock wave profile for some typical parameters. For the cases studied until now, the shock front has been extremely thin. Therefore, to resolve the front structure, we had to increase its width by increasing the viscosity and by causing the shock wave to travel faster, see Eqs. (18)–(20). The latter condition was achieved by multiplying $P(\rho)$ in Eq. (26) by a constant factor greater than unity (in this case equal to 9). We took $\rho_1=0.5$, $\rho_2=4.384$, and $\eta=0.25$. Figure 11 shows the resultant shock wave profile. It can be seen that on the higher density side, the profile is very abrupt, while on the lower-density side it is rather smooth. We observed the same feature in the time-dependent simulations of the shock wave formation (not shown graphically), choosing parameters accordingly to increase the front width.

Thus, we have found that in the nonlinear stage of the long-wavelength RCI dense (and therefore cool) plasma condensations (“drops of liquid”) are formed, surrounded by regions with a depleted density (“bubbles of vapor”). After some period of adjustment, accompanied by oscillatory plasma motions, the pressure in the condensations and in the surrounding lower density regions becomes uniform. Further evolution of the system depends on the boundary conditions. In the case of a free plasma inflow (an open system) the condensations expand, their boundaries representing the anomalous shock waves considered in the pre-

vious section. If the plasma inflow is not allowed (a closed system), stable equilibrium condensations develop, the boundaries of which represent contact discontinuities.

It should be noted that in reality the anomalous shock wave structure will not be determined by the small viscosity effects employed in our simulations mainly to avoid wave-breaking and stabilize the numerical scheme. Actually, the long-wavelength reduced equations for the RCI become invalid as steep density and temperature gradients develop in the process of instability and smaller spatial scales are introduced into the problem. Generally, the following dynamics is determined by two independent factors. The first of them is related to the force balance setting in (for the small spatial scales arising) on the same time scale as the thermal balance. The second factor is the heat conduction starting to act on the small spatial scales.

In the limiting case of a relatively small heat conduction, $\lambda_c \ll \lambda_a$, and a long-wavelength initial perturbation, $k \ll \lambda_a^{-1}$, it is the first factor which dominates. The corresponding nonlinear theory is not available yet. In essence, such a theory should match the long-wavelength solution outside the fronts with an intermediate-wavelength solution inside the fronts. One can assume that it is only the front width and structure that will be provided by a more complete theory, while all our “macroscopic” results for anomalous shock waves will remain intact, as is the case for shock waves in “normal” gas dynamics.

Alternatively, in the case of a large heat conduction, $\lambda_c \gg \lambda_a$, the whole nonlinear evolution can be described by the direct crossover equations, which are considered in the next section.

V. DIRECT CROSSOVER REGIME

In the case of a large heat conduction, the nonlinear RCI is described by the direct crossover equations (1), (2), (4) and (14). Let us start with possible nonuniform equilibria, $v = \partial/\partial t = 0$. We have

$$\rho \mathcal{L}(\rho, T) - \frac{d}{dx} \left(K \frac{dT}{dx} \right) = 0, \quad (30)$$

$$p = \frac{R}{\mu} \rho T = p_0 = \text{const}. \quad (31)$$

Note, that Eqs. (30) and (31) also describe the nonuniform equilibria of the *general*, unreduced problem [see Eqs. (1)–(4)]. Eliminating the density from Eq. (31), we have

$$\frac{d}{dx} \left(K \frac{dT}{dx} \right) - \lambda(T, p_0) = 0, \quad (32)$$

where

$$\lambda(T, p_0) = \frac{\mu p_0}{RT} \mathcal{L} \left(\frac{\mu p_0}{RT}, T \right). \quad (33)$$

Equation (32) (which should be solved subject to two boundary conditions) has been encountered in numerous works, including the theory and applications of the “reaction-diffusion” equation.^{31–33} Of particular interest are periodic solutions of Eq. (32) [nonlinear periodic

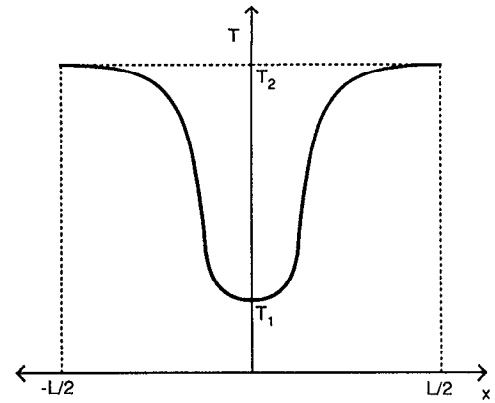


FIG. 12. A nonuniform equilibrium temperature profile, representing a solution of the force balance and thermal balance equations with the no-flux boundary conditions.

standing temperature (and density) waves], which normally exist if a uniform equilibrium is linearly unstable with respect to the RCI.¹⁹ Also, solutions consisting of an integer number of “segments” of such temperature waves and satisfying the no-flux boundary conditions, can usually be constructed unless the system is too short.³³ For example, for the case shown in Fig. 12, the solution can be written in an implicit form as

$$x = \pm \int_{T_1}^T \frac{K(T') dT'}{[2 \int_{T_1}^{T'} \lambda(\theta, p_0) K(\theta) d\theta]^{1/2}} \quad (34)$$

(where + and – refer to the positive and negative x , respectively), subject to condition

$$\int_{T_1}^{T_2} \lambda(T, p_0) K(T) dT = 0. \quad (35)$$

Condition (35) relates T_1, T_2 and p_0 . An additional condition relates T_1, T_2, p_0 and the interval length L :

$$\int_{T_1}^{T_2} \frac{K(T) dT}{[2 \int_{T_1}^T \lambda(\theta, p_0) K(\theta) d\theta]^{1/2}} = \frac{L}{2}. \quad (36)$$

Equations (34)–(36) determine possible equilibrium solutions, if any two of the four parameters, T_1, T_2, p_0 and L , are prescribed.

Since the equilibrium equations (30) and (31) are valid for the general, unreduced problem, described by Eqs. (1)–(4), the same is true for Eqs. (33)–(36). However, *stability* of these equilibria with respect to small perturbations, and their attainability from some “natural” initial conditions can differ for different limits of the RCI, as the corresponding *time-dependent* reduced equations are different. It has been shown^{34,35} that standing temperature waves are generally unstable in the framework of the *isobaric* intermediate- and short-wavelength reduced equations, when $\lambda_a^{-1} \ll k \ll \lambda_c^{-1}$. The instability is caused by the dominance of the $k=0$ mode [see Eq. (12) for the corresponding linear growth rate], which leads to “uniformization” of the system. This instability can be avoided in non-isobaric, confined plasmas, where the (uniform) plasma

pressure can vary in time.²² It is interesting to examine stability of the same equilibrium in the direct crossover model that we are considering now.

We performed numerical simulations with the direct crossover equations for different initial and boundary conditions. As we had to choose a convenient form for the heating-cooling function \mathcal{L} and also wanted to be able to recover the long-wavelength limit as $K \rightarrow 0$, we eliminated the temperature and rewrote Eq. (14) in the following form:

$$\kappa \frac{\partial^2}{\partial x^2} \left(\frac{p}{\rho} \right) - [p - P(\rho)] = 0, \quad (37)$$

where κ is the properly normalized heat conductivity, which we have assumed, for simplicity, independent of the temperature. Now, the direct crossover equations become Eqs. (1), (2) and (37).

For a negligible heat conductivity, we have $p = P(\rho)$, and the long-wavelength equations are recovered. Also, the linear theory of the RCI, following from Eqs. (1), (2) and (37), is correct. Indeed, for a small sinusoidal perturbation around a uniform equilibrium, the linear growth rate is the following:

$$\gamma_{dc} = \pm k \left(-\frac{dP/d\rho_0 + \kappa' (P_0/\rho_0) k^2}{1 + \kappa' k^2} \right)^{1/2}, \quad (38)$$

where $\kappa' = \kappa/\rho_0$. Returning to the heating-cooling function \mathcal{L} , we see that Eqs. (38) and (15) coincide if the normalized heat conductivity κ' is chosen properly, while other quantities are normalized so that $c_i = 1$.

Nonuniform equilibria are now described by the following equation:

$$\kappa \frac{d^2}{dx^2} \left(\frac{1}{\rho} \right) + \frac{P(\rho)}{\rho_0} - 1 = 0, \quad (39)$$

Eqs. (34)–(36) can be applied to Eq. (39) if one returns to $u = 1/\rho$ and substitutes in Eqs. (34)–(36)

$$T = u, \quad K = \kappa = \text{const}, \quad \text{and} \quad \lambda(\theta, p_0) = -\frac{P(1/\theta)}{p_0} + 1. \quad (40)$$

Equations (1), (2) and (37) were solved numerically for the cubic polynomial approximation (26) for $P(\rho)$. We used the same numerical algorithm as described in the previous section to solve Eqs. (1) and (2) for ρ and v . The pressure p was calculated at every time step from difference equations, approximating Eq. (37) and forming a tridiagonal system.

The first series of runs used the no-flux boundary conditions for the density and pressure (therefore, for the temperature as well), and zero velocity at the boundaries.

We started with the initial conditions (28) with $\rho_0 = 1.2$, $\epsilon = 0.001$, $k = 1$ and zero velocity. Figure 13 shows a series of density profiles in the case of $\kappa' = 0.1$ and a very small viscosity, $\eta = 0.005$. Initially, the density is almost uniform but its value in the central region grows with a corresponding reduction in the density in the periphery. Subsequent times show plasma condensation in the central

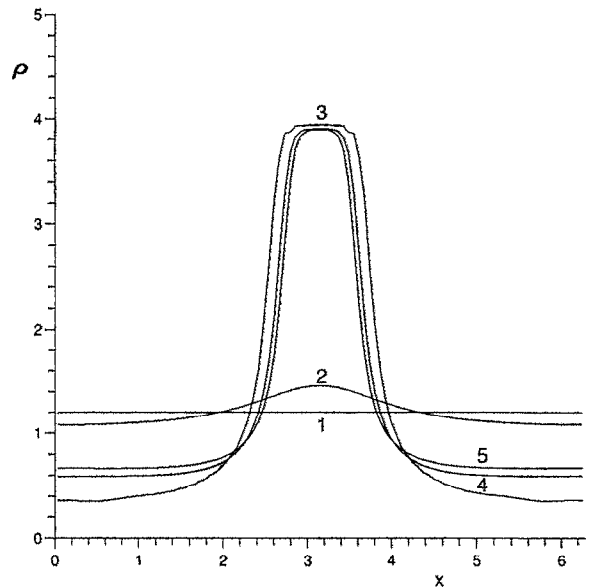


FIG. 13. Nonlinear evolution of the RCI in the direct crossover regime for the no-flux boundary conditions. Shown is the density profile versus time for the initial condition (28) with $\rho_0 = 1.2$, $\epsilon = 0.001$ and $k = 4$. The heat conduction parameter $\kappa' = 0.1$, while viscosity $\eta = 0.005$. The successive times are $t = 0$ (1), 20 (2), 50 (3), 100 (4), and 200 (5).

region. Unlike in the conduction-free cases, the transition between lower and higher density is gradual rather than abrupt. Close to $t = 200$, the pressure becomes uniform, the velocity vanishes (not shown graphically), and the system settles down to a stable nonuniform equilibrium. Therefore, the plasma condensation developing via the RCI in the direct crossover regime is indeed stable. The plasma is cooler in the condensation than in the periphery, so that the temperature profile looks like that shown in Fig. 12.

The heat conduction influences the form of the stable condensation. In the absence of conduction, steep temperature and density gradients develop (see the previous section). With the conduction, the final temperature and density profiles become smoother. Figure 14 shows several density profiles for different values of κ' and the same initial and boundary conditions as in Fig. 13. The viscosity was set to $\eta = 0.1$, a larger value, to ensure that the density profile after 200 time units has settled down to a very good approximation to the final state. Three distinct types of curve are apparent from Fig. 14, each corresponding to a particular range of values of κ' . For large values of conductivity (here illustrated by $\kappa' = 0.5$), the perturbed equilibrium is stable and the perturbation gradually dies away to leave a uniform equilibrium. (However, nonuniform equilibria may still result if a much larger perturbation were to be used, e.g., $\epsilon \sim 1$.) For intermediate values of the conductivity (illustrated here by $\kappa' = 0.35, 0.1$, and 0.025) the result is a nonuniform equilibrium with a single peak. The higher the conductivity, the smoother the profile and the lower the peak. The lower the conductivity, the closer the curve to the rectangular type of profile found in the absence of conduction. For still lower values of conduction

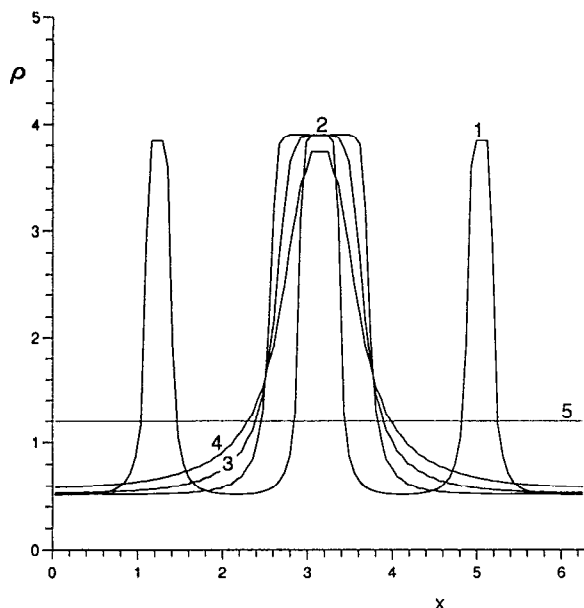


FIG. 14. The effect of heat conduction on the equilibrium condensation form in the direct crossover regime of the RCI with no-flux boundary conditions. The viscosity is $\eta=0.1$. Shown are the final density profiles for different values of κ' : 0.01 (1), 0.025 (2), 0.1(3), 0.35 (4), and 0.5 (5).

($\kappa=0.01$), the instability results in three density peaks rather than a single peak.

The main features of the numerical simulations can be explained by analyzing (i) the linear theory, Eq. (38), and (ii) the equilibrium solution (34) and conditions (35) and (36) as applied to Eq. (39) on the same interval $(0,2\pi)$. Let us start with the linear theory. The instability criterion predicted by Eq. (38) is the following:

$$\frac{dP}{d\rho_0} + \kappa' \frac{P_0}{\rho_0} k^2 < 0. \quad (41)$$

As we started from single-mode density perturbations (28), it was easy to check criterion (41), varying ρ_0 , κ and perturbation wave number k . Figure 15 shows the variation of the maximum density versus time for $\rho_0=1.5$ and $\kappa=0.1$, for six initial conditions of the form (28) with $\epsilon=0.001$ and $k=1, 2, \dots, 6$. It is seen from Fig. 15, that the modes with $k=1, 2$ and 3 are all unstable and grow until a new, nonuniform equilibrium is reached, while the modes with $k=4, 5$ and 6 are stable. Calculating the parameters entering criterion (41), we have $P_0=0.375$, $dP/d\rho_0=-0.25$ and $\kappa'=0.0667$, so that criterion (41) predicts that the modes $k=1, 2$ and 3 are unstable, while the higher modes are stable, in full agreement with the simulations. Note that, in the cases of instability, there are some oscillations present in the final states, but these are damped by a viscosity of 0.02.

Also, the stable condensation patterns developing in the time-dependent numerical simulations agree with those predicted by Eq. (39) for the equilibrium, if one takes the value of the equilibrium pressure p_0 from the simulations. Figure 16 shows the equilibrium solution of Eq. (39) with the no-flux boundary conditions for the case of $\kappa'=0.35$,

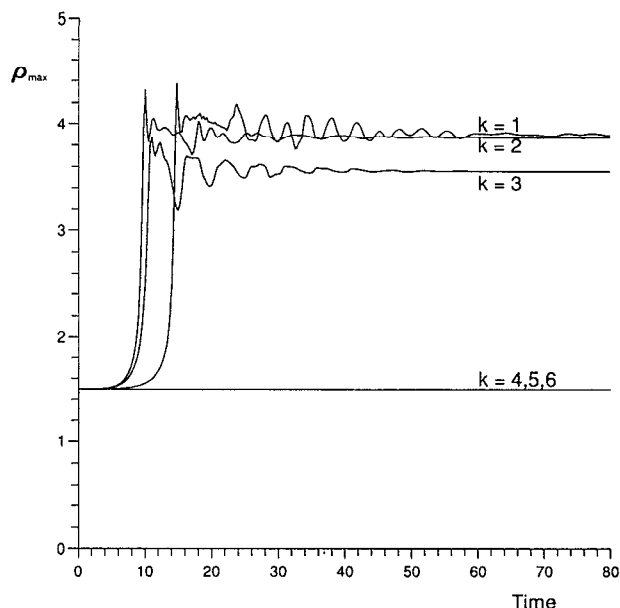


FIG. 15. The effect of the perturbation wavelength on the RCI in the direct crossover regime with no-flux boundary conditions. Shown is the maximum density versus time for each of the six modes with $k=1, 2, \dots, 6$. The initial conditions are in the form of Eq. (28) with $\epsilon=0.001$ and $\rho_0=1.2$.

obtained on the same interval $(0,2\pi)$ as the corresponding time-dependent simulations shown in Fig. 16. The value of $p_0=0.353$ was taken from the time-dependent simulation. A fairly good agreement between this profile and the corresponding one in Fig. 14 can be seen. It should be noted that comparing the profiles is not always easy, as the equilibrium solution is quite sensitive to small changes in p_0 , so that a small error in p_0 resulting from the time-dependent simulations can cause large errors in the form of the equilibrium profile. For this reason, it is more convenient to check the conditions (35) and (36), and we found that they hold with a good accuracy.

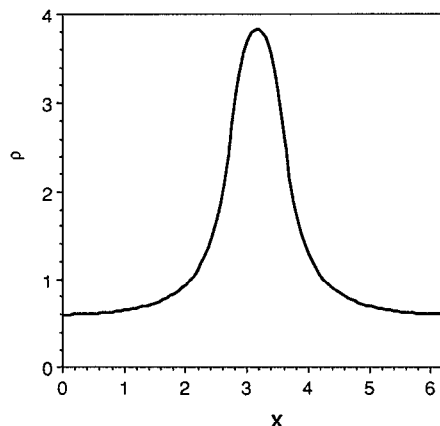


FIG. 16. Equilibrium density profile found from Eq. (39) on the same interval $(0,2\pi)$. The heat conduction parameter $\kappa'=0.35$. The equilibrium pressure $p_0=0.353$ was taken from the time-dependent simulations.

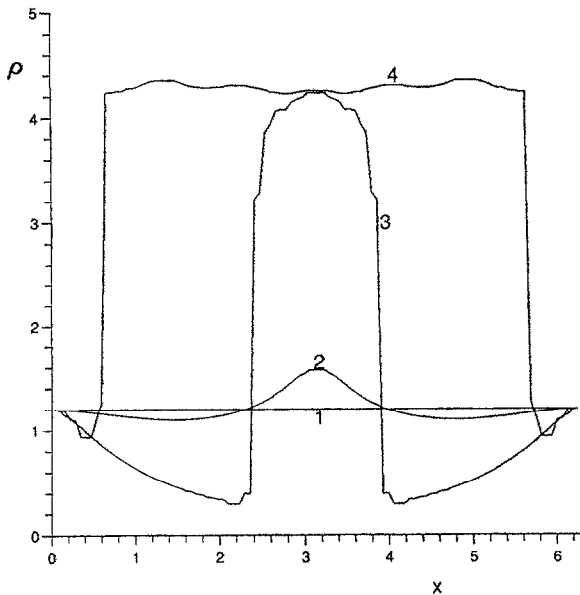


FIG. 17. Nonlinear evolution of the RCI in the direct crossover regime for boundary conditions allowing plasma inflow. Shown is the density profile versus time for the initial condition (29) with $v_0=0.1$. The heat conduction parameter $\kappa'=0.1$, the viscosity $\eta=0.005$. The successive times are $t=0$ (1), 10 (2), 20 (3), and 40 (4).

Boundary conditions allowing inflow of plasma lead to different results. An example is shown in Fig. 17. Here, we took $\kappa'=0.1$ and $\eta=0.005$, and started with a velocity perturbation of the form (29) with $v_0=0.1$ and $\rho_0=1.2$. It is seen that a central density maximum appears and grows before expanding out as more plasma enters the system. It is interesting to note that allowing plasma inflow appears to counteract the role of the heat conduction in eradicating steep gradients. Short-scale variations in Fig. 17 could be reduced by increasing the viscosity.

In addition to the “regular” initial perturbations (28) and (29), we also started with a multimode initial density perturbation,

$$\rho(x,t=0) = \rho_0 + \sum_{k=1}^N a_k \cos(kx) \quad (42)$$

with small positive and negative random mode amplitudes a_k and zero velocity. The number of modes N was usually set equal to 20; however, only those modes were important for which the criterion (41) predicted instability, while modes with higher k damped out. We performed simulations with $\rho_0=1.6$ and $\kappa=0.1$, when the unstable modes are those with $k=1, 2, 3$ and 4. For the no-flux boundary conditions, only regular equilibrium states with one, two or three density peaks finally developed, depending on the initial (random) choice of the mode amplitudes. As the values of the linear growth rates of the four unstable modes, γ_{dc} from Eq. (38), were fairly close to each other, the mode competition seemed to reflect the relative magnitudes of the initial mode amplitudes. Sometimes, however, nonlinear mode competition occurred, as a mode

dominating the initial stage of the growth was replaced at later times by another mode with a smaller k , which determined the final stable equilibrium.

VI. SUMMARY AND DISCUSSION

We have considered the nonlinear dynamics of one-dimensional RCI in the situation when a steady state thermal balance (with or without heat conduction) sets in on the shortest time scale, and then slower unstable gas dynamic motions occur. We have studied these motions analytically and numerically in the framework of two sets of reduced equations, the long-wavelength equations and the direct crossover equations.

We have shown that, in both limits, the nonlinear RCI results in formation of strongly nonuniform, regular patterns where dense and cool plasma regions are surrounded by rarefied and hot plasma regions. These patterns have been found to be standing or steadily expanding, depending on whether the boundary conditions disallow or allow plasma inflow into the system.

In the long-wavelength limit, the boundaries of the steady (equilibrium) condensations are contact discontinuities. The boundaries of expanding condensations represent anomalous shock waves with a monotonic density profile but a nonmonotonic pressure profile.

In the direct crossover regime, equilibrium condensations develop (which belong to the family of nonuniform equilibrium solutions of the force balance and thermal balance equations), if the plasma inflow is disallowed. We have seen numerically, that these condensations are stable. If plasma inflow is allowed, the condensations are expanding, their boundaries becoming much narrower, than those of the equilibrium condensations.

It is interesting to compare these results with those found recently in the intermediate- and short-wavelength limits of the RCI.^{20–22,34,35} In those limits, strongly nonlinear patterns also emerge, at least at some intermediate, radiative stage of the RCI. However, in open, isobaric systems, the patterns normally start to expand or shrink, and finally disappear, the plasma becoming uniform. The reason for this “uniformization” instability is, in essence, the domination of the modes with small k [see, for example, Eq. (12), showing the maximum linear growth rate of the RCI at $k=0$]. In the case of closed systems, when the pressure, being uniform, depends on time, the mode $k=0$ is forbidden by mass conservation, and so no uniformization occurs, and long-lived condensation patterns are possible.²² Returning to the long-wavelength and direct crossover regimes, one might assume that, as the linear growth rate (10) goes to zero as $k \rightarrow 0$, no uniformization will occur. The present results show that this assumption, based on the linear analysis, would be generally wrong, as we have found that, similar to the intermediate- and short-wavelength limits, stable equilibrium condensations develop only in the case of closed systems, while open systems finally show uniformization. These properties suggest a universal behavior for the one-dimensional nonlinear RCI in all wavelength ranges.

In summary, the reduced one-dimensional equations for the nonlinear RCI, although simplified considerably, help to gain insight into the nature of the instability, which is necessary for a correct interpretation of results of experiments, observations and more complete numerical models applied to specific problems.

ACKNOWLEDGMENTS

We are grateful to Dr. R. A. M. Van der Linden for helpful discussions on the linear theory of thermal instability and to M. Shots for technical help.

One of the authors (B.M.) gratefully acknowledges support from the Royal Society of London, which helped to make possible his visit to the Solar Theory Group in St. Andrews. Another author (C.D.C.S.) is grateful to the UK Science and Engineering Research Council for financial support.

- ¹L. Spitzer, *Physical Processes in the Interstellar Medium* (Wiley, New York, 1978).
²K. Davidson, *Astrophys. J.* **171**, 213 (1972).
³E. Tandberg-Hanssen, *Solar Prominences* (Reidel, Dordrecht, 1974); E. R. Priest (editor), *Dynamics and Structure of Quiescent Solar Prominences*, *Astrophysics and Space Science Library* (Kluwer Academic, Dordrecht, 1989), Vol. 150.
⁴J. L. Terry, E. S. Marmor, and S. M. Wolfe, *Bull. Am. Phys. Soc.* **26**, 886 (1981); B. Lipshultz, *J. Nucl. Mater.* **145**, 15 (1987).
⁵R. S. Pease, *Proc. R. Soc. London Ser. B* **70**, 11 (1957); S. I. Braginskii, *Zh. Exp. Teor. Fiz.* **33**, 645 (1957) [*Sov. Phys. JETP* **6**, 494 (1958)]; J. D. Lawson, *J. Nucl. Energy C* **1**, 31 (1959); V. V. Neudachin and P. V. Sasorov, *Nucl. Fusion*, **31**, 1053 (1991).
⁶E. N. Parker, *Astrophys. J.* **117**, 431 (1953).
⁷G. B. Field, *Astrophys. J.* **142**, 531 (1965).
⁸S. B. Pikel'ner, *Astron. Zh.* **44**, 915 (1967) [*Sov. Astron.* **11**, 737 (1968)].
⁹G. B. Field, D.W. Goldsmith, and H. J. Habing, *Astrophys. J. (Lett.)* **155**, L149 (1969).
¹⁰D. W. Goldsmith, *Astrophys. J.* **161**, 41 (1970).

- ¹¹E. Hildner, *Solar Phys.* **35**, 123 (1974).
¹²E. S. Oran, J. T. Mariska, and J. P. Boris, *Astrophys. J.* **254**, 349 (1982).
¹³Y. Mok, J. F. Drake, D. D. Schnack, and G. Van Hoven, *Astrophys. J.* **359**, 228 (1990); Y. Mok, D. D. Schnack, and G. Van Hoven, *Solar Phys.* **132**, 95 (1991).
¹⁴D. McCarthy and J. F. Drake, *Phys. Fluids B* **3**, 22 (1991).
¹⁵J. T. Karpen, S. K. Antiochos, J. M. Picone, and R. B. Dahlburg, *Astrophys. J.* **338**, 493 (1989).
¹⁶L. Sparks, G. Van Hoven, and D. D. Schnack, *Astrophys. J.* **353**, 297 (1990).
¹⁷B. I. Meerson and P. V. Sasorov, *Zh. Eksp. Teor. Fiz.* **92**, 531 (1987) [*Sov. Phys. JETP* **65**, 300 (1987)].
¹⁸P. V. Sasorov, *Pis'ma Astron. Zh.* **14**, 306 (1988) [*Sov. Astron. Lett.* **14**, 129 (1988)].
¹⁹B. Meerson, *Astrophys. J.* **347**, 1012 (1989).
²⁰A. M. Dimits and B. Meerson, *Phys. Fluids B* **3**, 1420 (1991).
²¹B. Meerson, E. R. Priest, and C. D. C. Steele, *Geophys. Astrophys. Fluid Dyn.* **71**, 243 (1993).
²²I. Aranson, B. Meerson, and P. V. Sasorov, *Phys. Rev. E* **47**, 4337 (1993).
²³A. G. Doroshkevich, and Ya. B. Zel'dovich, *Zh. Eksp. Teor. Fiz.* **80**, 801 (1981) [*Sov. Phys. JETP* **53**, 405 (1981)].
²⁴Ya. B. Zel'dovich and I. D. Novikov, *The Structure and Evolution of the Universe, Relativistic Astrophysics* (University of Chicago Press, Chicago, 1983), Vol. 2.
²⁵B. A. Trubnikov and S. K. Zhdanov, *Phys. Reports* **155**, 137 (1987).
²⁶P. V. Sasorov, *Astron. Zh.* **52**, 106 (1975) [*Sov. Astron.* **19**, 62 (1975)].
²⁷H. Scheffler and H. Elsässer, *Physics of the Galaxy and Interstellar Matter* (Springer-Verlag, Berlin, 1987).
²⁸C. Kittel and H. Kroemer, *Thermal Physics* (Freeman, San Francisco, 1980), p. 290.
²⁹L. D. Landau and E. M. Lifshitz, *Fluid Mechanics* (Pergamon, London, 1959).
³⁰J. P. Boris and D. L. Book, *Methods Comput. Phys.* **16**, 85 (1976).
³¹D. A. Frank-Kamenetskii, *Diffusion and Heat Transfer in Chemical Kinetics* (Plenum, New York, 1969).
³²P. Fife, *Mathematical Aspects of Reacting and Diffusing Systems, Lecture Notes in Biomathematics* (Springer-Verlag, New York, 1979), Vol. 28.
³³J. D. Murray, *Mathematical Biology* (Springer-Verlag, Berlin, 1989).
³⁴B. Meerson and N. Persky (private communication, 1992).
³⁵C. Elphick, O. Regev, and N. Shaviv, *Astrophys. J.* **392**, 106 (1992).